arXiv:nucl-th/9812034v2 2 Mar 1999

Elliptic Flow and HBT in non-central Nuclear Collisions

Henning Heiselberg
NORDITA, Blegdamsvej 17, DK-2100 Copenhagen Ø, Denmark

Anne-Marie Levy
Niels Bohr Institute, Blegdamsvej 17, DK-2100 Copenhagen Ø, Denmark

Elliptic flow and HBT are studied for non-central relativistic nuclear collisions. Azimuthal asymmetries show up in both elliptic flow and HBT radii and are calculated in both collisionless and hydrodynamic limits relevant for peripheral and central collisions respectively. Determining the reaction plane and measuring the HBT radii as function of the angle between the reaction plane and the particle momenta can determine the physical quantities as source sizes, deformations, emission times, duration of emission and opacities. Comparison to SPS data and predictions for RHIC and LHC energies are given. The centrality dependence with and without a phase transition to a quark-gluon plasma is discussed - in particular, how the physical quantities are expected to display a qualitative different behavior in case of a phase transition.

PACS numbers: 25.75.+r, 25.70.Pq

I. INTRODUCTION

The azimuthal asymmetries in momentum spectra usually referred to as directed and elliptic flow are large in nuclear collisions at intermediate energies [1] which allows experimental reconstruction of the reaction plane. Also in relativistic nuclear collisions at the AGS [2] and SPS [3] anisotropic flow has been found in semi-central collisions. Likewise, HBT analyses has successfully been made, however, so far without simultaneous reconstruction of the reaction plane. The statistics may permit this in the near future and the prospects looks good for the RHIC and LHC colliders, where the multiplicities are much higher and the number of pairs entering HBT analyses grow with the multiplicity squared. Particle interferometry (HBT [4]) may also show source asymmetries [5,6] spatially and complement the momentum space information of flow. Earlier studies of directed and elliptic flow by hydrodynamics [7] as well as by the cascade code RQMD [8,9] has been compared to AGS and SPS data with some success. The data shows interesting transverse momentum and rapidity dependences for pions and protons that cannot be explained by these models.

The aim of this work is to return to the basic physics that leads to azimuthal anisotropies in semi-central collisions in both coordinate and momentum space which are relevant for the HBT radii and anisotropic flow respectively. We shall derive simple analytical formulas for elliptic flow and HBT radii in both the collisionless and hydrodynamic limits relevant for peripheral and near-central collisions respectively. A combined analysis of HBT and anisotropic flow yields detailed information on the particle source at freeze-out as well as the expansion from the initial collision and up to freeze-out. General properties as the initial geometry, shadowing effects, expansion and freeze-out can be determined through detailed measurements on source sizes, deformations, lifetimes, duration of emission, opacities, transverse and elliptic flow. We discuss the effects of a phase transition occurring when the energy densities become high enough to form a quark-gluon plasma at some semi-centrality. The centrality, E_T or dN/dy dependence of a number of measurable quantities as the ratio of the elliptic flow to the deformation, duration of emission, opacity, etc. may display an interesting behavior.

The paper is organized as follows. First we describe the geometry of semicentral relativistic nuclear collisions and discuss the azimuthal asymmetries and deformations of the overlap zone in sec. II. In sec. III we calculate elliptic flow in the collisionless and hydrodynamic limits relevant for peripheral and near central collisions respectively and compare to recent SPS data [3]. HBT radii are calculated for deformed sources in sec. IV. In sec. V we discuss the qualitative behavior of a number of physical quantities from elliptic flow to HBT radii - with and without a phase transition to a quark-gluon plasma. Finally a summary is given.

II. GEOMETRY OF SEMI-CENTRAL COLLISIONS

In non-central nuclear collisions the reaction plane breaks azimuthal symmetry. The asymmetry decreases with centrality and vanish for the very central collisions (see Fig. 1).

We will use the term *centrality* as impact parameter b in the collision. It is not a directly measurable quantity but is closely correlated to the transverse energy produced E_T, the measured energy in the zero degree calorimeter and the total particle rapidity density dN/dy. The latter is again approximately proportional to the number of participating nucleons

$$N_{part} = \int_{overlap} \left[\rho(\mathbf{r}+\frac{\mathbf{b}}{2}) + \rho(\mathbf{r}-\frac{\mathbf{b}}{2})\right] d^3r\,. \tag{1}$$

The number of participants for colliding two spherical nuclei of radius R is shown in Fig. 2 as function of impact parameter.

The standard geometry has the z-direction along the longitudinal or beam axis and the x-direction along the impact parameter **b**. Thus (x,z) constitutes the *reaction plane* and (x, y) the transverse direction with y perpendicular to the reaction plane. It is convenient — also for comparison to HBT analyses — to employ gaussian parametrizations for anisotropic sources in both transverse directions

$$S_\perp(\mathrm{x},\mathrm{y}) = \frac{1}{2\pi R_x R_y} \exp\left(-\frac{\mathrm{x}^2}{2R_x^2} - \frac{\mathrm{y}^2}{2R_y^2}\right)\,. \tag{2}$$

Here, the gaussian transverse sizes R_x and R_y increase with time as the source expands after the collision. The initial transverse radii, i.e., the rms radii of the overlap zone weighted with nuclear thickness functions, are shown in Fig. 2. For HBT the relevant radii are, however, those at freeze-out which are larger due to expansion as discussed below.

The azimuthal asymmetry or "deformation" of the source can be defined as the relative difference between the gaussian radii squared

$$\delta \equiv \frac{R_y^2 - R_x^2}{R_y^2 + R_x^2}\,. \tag{3}$$

A simple estimate can be obtained from the full transverse extent of the initial overlap of two nuclei of mass number A and radius $R_A \simeq 1.2A^{1/3}$ colliding with impact parameter b (see Fig. 1). They are: $R_x = R_A - b/2$ and $R_y = \sqrt{R_A^2 - b^2/4}$, and the corresponding deformation is

$$\delta = \frac{b}{2R_A}\,. \tag{4}$$

The rms radii of the nuclear overlap zone weighted with longitudinal thicknesses results in deformations (see Fig. 2) that are slightly smaller than Eq. (4) at semicentral collisions. However, as the source expands the deformation $\delta \simeq (R_y - R_x)/(R_y + R_x)$ decreases for two reasons.

Firstly, the expansion increase $(R_x + R_y)$ as is found in HBT and Coulomb analyses [11]. Secondly, $(R_y - R_x)$ decrease because the average velocities are larger in the x- than y-direction. The latter is a consequence of the experimentally measured positive elliptic flow ($v_2 > 0$ in Eq. (5)) in relativistic nuclear collisions where shadowing is minor [2,3]. Measuring the decrease of the deformation with centrality will reveal important information on the expansion up to freeze-out. For very peripheral collisions, where only a single nucleon-nucleon collision occurs, the source must be azimuthally symmetric, i.e., the deformation must vanish and therefore Eq. (4), which assumes continuous densities, breaks down.

III. ELLIPTIC FLOW

The reaction plane, which breaks azimuthal symmetry, has been successfully determined in non-central heavy ion collisions from intermediate up to ultrarelativistic energies [3]. The particle spectra are expanded in harmonics of the azimuthal angle ϕ event-by-event [7]

$$\begin{aligned} E\frac{dN}{d^3p} &= \frac{dN}{p_t dp_t dy d\phi} = \int d^4x n(x,p) \\ &= \frac{dN}{2\pi p_t dp_t dy} \times [1 + 2v_1\cos(\phi-\phi_R) \\ &\qquad +2v_2\cos 2(\phi-\phi_R) \,+ ...]\,, \end{aligned} \tag{5}$$

where $n(x,p)$ is the particle distribution function in space and time $x = \mathbf{r}, t)$, and ϕ_R is the azimuthal angle of the reaction plane. Assuming that the experimental uncertainties in event plane reconstruction can be corrected for, each event can be rotated such that $\phi_R = 0$. The asymmetry decreases with centrality (see Fig. 1+2 and Eq. (4)) and vanish for the very central collisions which are cylindrical symmetric. The expansion parameters are v_1 for *directed* flow and v_2 for *elliptic* flow.

At Bevalac energies where the directed flow in semicentral collisions of heavy nuclei is up to 20 degrees [1] with respect to the beam line. The directed flow decrease with energy and is only $\sim 1/20$ degree at SPS energies [3]. At AGS and SPS energies there are now very accurate measurements for protons, positive and negatively charged pions as function of rapidity and transverse momentum. [2,3] Both pions and protons are found to have elliptic flow in the reaction plane at AGS [2] and SPS [3] energies, i.e., $v_2 > 0$ for all rapidities and transverse momenta. At SPS $v_2 \lesssim 0.1$ for protons but smaller for pions as well as for protons at AGS. We refer to [7] for recent results on flow in relativistic heavy ion collisions.

At collision energies below a few GeV the nuclei shadow the collision region in the reaction plane. Consequently, the flow is "squeezed out" in the y-direction, i.e., $v_2 < 0$. At ultrarelativistic energies Lorentz contraction of the nuclei reduce the amount of shadowing at midrapidities and one finds that $v_2 > 0$. We will in the following restrict ourselves to ultrarelativistic energies and midrapidities where effects of shadowing are minor.

A. Collisionless limit/Peripheral collisions

In peripheral collisions the nuclear overlap zone is small and at relativistic energies the expansion is fast. Produced particles can therefore escape frow the collision zone almost without interacting with the other particles, i.e., the system is close to free streaming and the collisionless limit. We can then calculate the first order correction to free streaming from particle collisions. This approximation is valid when the particle mean free paths $\lambda_{mfp} \simeq (\sigma\rho)^{-1}$ are larger than the overlap zone $R_{x,y}(b)$. For pions and protons λ_{mfp} of order a few fm's for particle densities of order nuclear saturation densities, i.e., comparable to source sizes in semi-central collisions. If we assume that particles initially are produced azimuthally symmetric in momentum space but not in coordinate space, these subsequent interactions with comovers will produce an azimuthally asymmetric momentum distribution because the source is azimuthally asymmetric spatially.

We shall not attempt to describe the initial hard nucleon-nucleon collisions, the fragmentation or particle production. Our starting point is some initial conditions at formation time $\tau_0 \sim 1$ fm/c and consider the subsequent scatterings between comovers described by the Boltzmann or Nordheim [12] equation

$$\left(\frac{\partial}{\partial t} + \mathbf{v}_p \cdot \nabla\right) n_1 = \int \frac{d^3p_2}{(2\pi)^3} d\Omega\, v_{12} \frac{d\sigma}{d\Omega} \times \left[n_3 n_4 (1 \pm n_1)(1 \pm n_2) - n_1 n_2 (1 \pm n_3)(1 \pm n_4)\right] . \quad (6)$$

Here, $n_i = n(r_i, p_i, t)$ is the particle distribution function and $d\sigma/d\Omega$ is the cms differential cross section for scattering particles $1 + 2 \to 3 + 4$. Stimulated emission and Pauli Blocking are including by the $\pm$ factors.

To evaluate the effect of collisions on the distribution function in (6) we assume Bjorken scaling $v_z = z/t$ initially at invariant time τ_0. As usual, the space-time rapidity is $\eta = (1/2)\log((t + z)/(t - z))$ and $\tau = \sqrt{t^2 - z^2}$ is the invariant time. The transverse particle density distribution is approximated by simple gaussians as in Eq. (2). The free streaming distribution is then at later times

$$n(x, p) = f_0(p_\perp, p'_z)\, S_\perp(\mathbf{r}_\perp - \mathbf{v}_\perp(\tau - \tau_0)) . \quad (7)$$

Here, $\mathbf{r}_\perp = (\mathrm{x}, \mathrm{y})$ is the transverse radius, $\mathbf{v}_\perp = (v_x, v_y)$ the transverse velocity. The local particle momentum distribution, $f_0(\mathbf{p})$, is discussed in detail in Appendix A; in the final result it can be rewritten in terms of final measured momentum distributions, dN/d^2p_t. The scaled longitudinal momentum

$$p'_z = \frac{\tau}{\tau_0} m_\perp \sinh(\eta - y) , \quad (8)$$

takes the free streaming longitudinally into account [13]. Transverse expansion of the source is incorporated by the Galilei transformations of the transverse coordinates (x, y). Note, that the momentum distribution of produced particles is azimuthally symmetric at initial production time τ_0. The detailed form of f_0 will not be necessary for the evaluation of elliptic flow or HBT radii. It is sufficient to know the rapidity density dN_j/dy of the scattering particles j.

In the collisionless limit we can now insert the free streaming distribution function in the collision term in order to calculate the first order correction to the distribution function from (6). This correction provides the deviation from cylindrical symmetry and directly leads to elliptic flow, v_2^i, for particle species $i = \pi, p, K, ...$, as is evaluated in detail in Appendix A

$$v_2^i = \frac{\delta}{16\pi R_x R_y} \sum_j \langle v_{ij} \sigma_{tr}^{ij} \rangle \frac{dN_j}{dy} \frac{v_{i\perp}^2}{v_{i\perp}^2 + \langle v_{j,\perp}^2 \rangle} . \quad (9)$$

Here, v_i is the particle, v_j the scatterer and v_{ij} the relative velocity. The averages $\langle .. \rangle$ refers to averaging over scatterer momenta p_j. Since it is the momentum transfer in collisions, that deforms the particle momentum distribution around cylindrical symmetry, it is naturally the *momentum transport cross section* σ_{tr}^{ij} that enters. The elliptic flow parameter is proportional to the deformation and neccessarily vanishes for an azimuthally symmetric source.

The other important factors in the elliptic flow are

$$\tilde{\sigma}_{ij} \equiv \frac{dN_j}{dy} \frac{\langle v_{ij} \sigma_{ij} \rangle}{\pi R_x R_y} . \quad (10)$$

It is the cross section times a transverse particle density and thus describes the effective "opacity" of the source for particles i scattering with particles j.

It is remarkable that the initial time τ_0 does not enter in (9). The τ_0-dependence cancels to first approximation as explained in appendix A, due to a compensation between the densities decreasing with expansion time and that scatterings only lead to asymmetries as they pass through the source with time. The physical reason for the "late time" dominance in elliptic flow is that a particle has to travel a distance $\sim R$ before it feels the source deformation, i.e., whether it moves in the x-direction, or in the y− direction which differs by a distance $R_y - R_x \simeq \delta R$. This also explains why the elliptic flow is proportional to $v_{i\perp}^2$. The slow particles do not travel far enough to feel the deformation before the source has expanded - by velocity $v_{ij,\perp}$.

The centrality dependence of the elliptic flow can be estimated from Eq. (9). In high energy nuclear collisions the total multiplicity dN/dy scales approximately with the number of participating nucleons, Eq. (1) which is shown in Fig. 2 as function of impact parameter together with $R_x(b)$, $R_y(b)$ and $\delta(b)$. The resulting centrality dependence of v_2 from Eq. (9), assuming that dN_j/dy also are proportional to the number of participants, is shown in Fig. 2 as well. It vanishes for central and grazing collisions, has a maximum for peripheral collisions $b \simeq 1.5R$

and decreases almost linearly with increasing centrality. A very similar behavior was found in the hydrodynamic calculations of Ollitrault [7].

B. Hydrodynamic limit/Semi-central collisions

In semi-central collisions at relativistic energies, where large particle densities are produced, rescatterings are abundant and the hydrodynamic limit (see, e.g., [7]) is better than the collisionless — at least up to freeze-out.

We will here attempt to extract some general features in the hydrodynamic limit and derive an approximate analytical formula for the elliptic flow. Instead of introducing two independent transverse flow velocities (u_x, u_y) we relate the transverse flow to the spatial deformation by the plausible assumption that the transverse flow is *equipotential, i.e., perpendicular to and with constant magnitude on equi-density surfaces.* This assumption is obvious for cylindrical symmetric sources. Also for a very deformed source, which appears as a slab in one transverse direction, the flow is perpendicular to most of the freeze-out surface. For a rectangular source the flow is initially also perpendicular to the surface in all directions but as the source expands deviations may occur at the corners. Concerning the constant magnitude of the transverse flow on the freeze-out surface, that may be justified for deformed sources by the following observation. In the Riemann solution to 1D hydrodynamics, the flow velocity only depends on time and the relative distance from the initial surface, i.e., $(r-R)$. As shown in [14] the Riemann solution is also a very good approximation to the cylindrical case with longitudinal Bjorken scaling with an additional scaling factor of $(\tau_0/\tau)^{c_s^2}$ for temperatures. For the slab or the rectangular source, the magnitude flow velocities will therefore only depend on the relative distances from the initial transverse radii, i.e., $(\mathrm{x}-R_x)$ or $(\mathrm{y}-R_y)$. How good this approximation is in general for near central relativistic heavy ion collisions should, of course, be checked by solving full 3D hydrodynamics.

With the simplifying approximation of equipotential flow we can calculate the resulting particle spectrum for a locally thermal distribution $e^{p\cdot u/T}$ with longitudinal Bjorken flow,

$$u = (\gamma\cosh(\eta), \gamma\sinh(\eta), \mathbf{u}_\perp), \qquad (11)$$

where $\gamma = \sqrt{1+u_\perp^2}$. The transverse extent is parametrized by (2). With these assumptions the resulting momentum distribution can be found by integrating over the deformed equipotential surfaces as described in Appendix B. The asymmetric term gives the elliptic flow

$$v_2 = \left\{ \begin{array}{ll} \frac{1}{4}\frac{p_\perp^2\langle u_\perp^2\rangle}{T^2}\delta & ,\ p_\perp u_\perp \ll T \\ \frac{1}{2}(\frac{p_\perp\langle u_\perp\rangle}{T}-1)\delta & ,\ p_\perp u_\perp \gg T \end{array} \right\} . \qquad (12)$$

It is expected that the elliptic flow is proportional to the deformation which vanishes for central collisions. The relevant deformation is now at freeze-out where the radii which may differ from the initial transverse radii as discussed above.

The elliptic flow of Eqs. (12) depends only indirectly on the unknown quantities as the initial densities, equation of state, expansion, etc. through the average transverse flow, temperature and deformation. The transverse flow and temperature can be extracted independently from transverse flow analyses by looking at the particle mass dependence of average $p_\perp$ as suggested in [15] or by measuring the *apparent temperatures* [16], i.e., the inverse of the $m_\perp$ slopes. As shown in Appendix C the apparent temperature obtained from exponential fits to transverse mass spectra of massive particles is

$$T_{app} \simeq T + \frac{1}{2}m\langle u_\perp^2\rangle , \qquad (13)$$

for large particle masses m and small transverse flow. Experimentally, the apparent temperatures scales approximately linearly with the masses of the pion, kaon, proton, and deuterium in central $S+S$ and $Pb+Pb$ collisions at AGS and CERN [16] energies. From the experimental slopes $2dT/dm$ we thus obtain $\langle u_\perp^2\rangle \simeq 0.15c^2$ and $0.3c^2$ for central $S+S$ and $Pb+Pb$ collisions at SPS energies.

It is instructive to compare to another type of hydrodynamic flow parametrized by two transverse flow velocities

$$\mathbf{u}_\perp = (u_x x/R_x, u_y y/R_y) . \qquad (14)$$

The resulting particle distribution can be calculated along the lines of Appendix B. The resulting elliptic flow is for small transverse momenta

$$v_2 = \left\{ \begin{array}{ll} \frac{1}{16}\frac{p_\perp^2}{T^2}(\langle u_x^2\rangle - \langle u_y^2\rangle) & ,\ p_\perp u_\perp \ll T \\ \frac{1}{8}(\frac{p_\perp\langle u_\perp\rangle}{T}-1)\frac{\langle u_x^2\rangle-\langle u_y^2\rangle}{u_\perp^2} & ,\ p_\perp u_\perp \gg T \end{array} \right\} . \qquad (15)$$

Comparing Eq. (15) to the elliptic flow data for protons of Fig. 3 we can estimate the difference $\langle u_x^2\rangle - \langle u_y^2\rangle \simeq 0.015$, i.e., an order of magnitude smaller than the average transverse flow $u_\perp^2 \simeq (u_x^2+u_y^2)/2 \simeq 0.15$ that was estimated from Eq. (13). The elliptic flow of Eq. (15) is not related to the spatial deformation as was the equipotential flow and therefore its predictive power is less.

C. Comparison to elliptic flow at SPS energies

The elliptic flow as estimated by the collisionless and hydrodynamic limits may be compared to NA49 data at SPS energies [3] taken for semicentral $Pb+Pb$ collisions ($b \simeq R \simeq 7fm$). The $p_\perp$ dependence of v_2 for pions and protons is measured at forward rapidities $4 \le y \le 5$. We can take the free cross sections and ignore medium effects since the densities are small at late times when rescatterings lead to anisotropies (see Appendix A). The relevant scattering cross section σ^{ij} is that where nucleons act as scatterers because they are heavier than e.g.

pions and thus deflect more. Furthermore, typical scattering cross sections $\sigma^{\pi N}$ are larger than $\sigma^{\pi\pi} \simeq 10$mb [17]. The former is dominated by the Δ-resonance. Averaging of scatterer momenta we estimate $\sigma^{\pi N} \simeq 30$mb and $\sigma^{NN} \simeq 40$mb. The transport cross sections are smaller because forward scattering without momentum loss should not be included. For an estimate we simply take the transport cross section as half of the total cross section. The relevant rapidity density is that of nucleons which we take from the NA49 experiment $dN_N/dy \simeq 30$. From Fig. 2 we obtain $R_x \simeq 2fm$, $R_y \simeq 3fm$ and $\delta \simeq 0.4$ for $b = R$. The resulting elliptic flow is shown in Fig. 3 for pions and protons. The estimates in the collisionless limit of Eq.(9) give a reasonable description of both the magnitude and $p_\perp$-dependence for both pions and protons. Furthermore, the measured elliptic flow is largest at midrapidities and is approximately proportional to dN/dy as predicted by Eq.(9).

In the hydrodynamic limit transverse flow couples to $p_\perp$ and elliptic flow is therefore expected to be the same for all particles at the same $p_\perp$. The elliptic flow can differ if various particle species freeze-out at different temperatures or resonance decays affect the final distributions. The elliptic flow is shown in Fig. 3 for equipotential flow, Eq. (12), with $T \simeq 160$ MeV and $\langle u_\perp^2 \rangle \simeq 0.15c^2$ as estimated above. An excellent fit to the magnitude and $p_\perp$ dependence of proton elliptic flow can be obtained with a deformation at freeze-out of $\delta \simeq 0.07$. This value for the deformation is a factor ~ 6 smaller than the initial deformation of the collision zone. It is expected to be smaller due to expansion between initial collision and freeze-out but a full 3+1 dimensional hydrodynamic calculation is needed in order to chech the magnitude of the deformation as well as the validity of equipotential flow. The deformation at freeze-out can in principle be extracted from HBT analyses as shown in the following section and would thus be an important independent check.

The pion elliptic flow cannot be explained in the hydrodynamic limit as it differs from proton flow and does not have the right $p_\perp$ dependence. It is curious that the magnitude of the pion elliptic flow lies between the collisionless and hydrodynamic limit. This may indicate that semi-central $Pb+Pb$ collisions at SPS energies lies between these two limits as one would expect since the particle mean free paths are a few $fermi$'s — comparable to the transverse source sizes for $b = R_{Pb} \simeq 7$ fm/c. Comparing the $p_\perp$-dependence of elliptic flow for pions and protons would reveal the change from collisionless expansion to hydrodynamic flow. In the collisionless limit the pion and proton elliptic flow differ whereas in the hydrodynamic limit they should become the same as shown in Fig. 3.

Calculations with the RQMD and VENUS models (see [3,9] for detailed comparisons) give an almost rapidity independent elliptic flow which underpredicts the SPS data by a factor $\sim 2-4$ at midrapidity. The smaller elliptic flow in RQMD at midrapidities is attributed to "preequilibrium softening" [8]. Hydrodynamic models results in corresponding values for v_2 which are ~ 4 times larger for an ideal ($c_s^2 = 1/3$) pion gas and ~ 2 times larger when a first order phase transition at $T_c \sim 150$MeV is included [7].

It is curious that the elliptic flow is less than a few percent in relativistic nuclear collisions in comparison to the initial spatial deformations which are of order $\delta \simeq 50\%$ in semi-central collisions. The reason can be understood in both the collisionless and hydrodynamic limits due to the limited time and distances that particles have to rescatter and develop asymmetric collective flow before they freeze-out. In other words, the scatterings that lead to asymmetric flow occur at late times where the source and scatterers have already expanded and reduced the initial deformation.

The elliptic flow at RHIC and LHC energies would be large if one simply extrapolates from intermediate, AGS and SPS energies [3] However, at the intermediate energies shadowing is responsible for a negative v_2 (squeeze-out) and is still felt at AGS energies. At SPS energies it may also affect the forward rapidity data $4 < y < 5$ where the projectile nucleus is less Lorentz contracted and thus shadow. But at central rapidities at SPS and higher energies shadowing is minor due to the strong Lorentz contraction of nuclear sizes. Therefore, v_2 is unaffected by shadowing from SPS and up in energy, i.e., constant rather than increase as given by a naive extrapolation from intermediate, AGS and SPS energies. However, since dN/dy and probably also the transverse flow is larger at RHIC and LHC energies, we may expect stronger elliptic flow. On the other hand, the expansion reduces the deformation and thus also the elliptic flow.

IV. HBT

A brief description of interferometry will be given describing how to calculate correlation functions and HBT radii from a given source. The HBT radii will then be calculated for deformed sources - transparent as well as opaque. A brief description of results were presented in [18]. A comparison is given and the advantages of a combined HBT and elliptic flow analysis is discussed.

Particle interferometry was invented by Hanbury-Brown & Twiss (HBT) for stellar size determination [4] and is now employed in nuclear collisions [20–24,10,19]. It is a very powerful method to determine the 3-dimensional source sizes, life-times, duration of emission, flow, etc. of pions, kaons, etc. at freeze-out. Since the number of pairs grow with the multiplicity per event squared the HBT method will become even better at RHIC and LHC colliders where the multiplicity will be even higher.

The standard HBT method for calculating the Bose-Einstein correlation function from the interference of two identical particles is now briefly discussed. For a source of size R we consider two particles emitted a distance

$\sim R$ apart with relative momentum $\mathbf{q} = (\mathbf{k}_1 - \mathbf{k}_2)$ and average momentum, $\mathbf{K} = (\mathbf{k}_1 + \mathbf{k}_2)/2$. Typical heavy ion sources in nuclear collisions are of size $R \sim 5$ fm, so that interference occurs predominantly when $q \lesssim \hbar/R \sim 40$ MeV/c. Since typical particle momenta are $k_i \gtrsim K \sim 300$ MeV/c, the interfering particles travel almost parallel, i.e., $k_1 \simeq k_2 \simeq K \gg q$. The correlation function due to Bose-Einstein interference of identical spin zero bosons as $\pi^\pm\pi^\pm$, $K^\pm K^\pm$, etc. from an incoherent source is (see, e.g., [23])

$$C_2(\mathbf{q},\mathbf{K}) = 1 \pm \left| \frac{\int d^4x\, S(x,\mathbf{K})\, e^{iqx}}{\int d^4x\, S(x,\mathbf{K})} \right|^2 , \qquad (16)$$

where $S(x,\mathbf{K})$ is the source distribution function describing the phase space density of the emitting source.

Experimentally the correlation functions are often parametrized by the gaussian form

$$C_2(q_s,q_o,q_l) = 1 + \lambda \exp[-q_s^2 R_s^2 - q_o^2 R_o^2 - q_l^2 R_l^2 \\ -2q_o q_s R_{os}^2 - 2q_o q_l R_{ol}^2] \, . \qquad (17)$$

Here, $\mathbf{q} = \mathbf{k}_1 - \mathbf{k}_2 = (q_s, q_o, q_l)$ is the relative momentum between the two particles and $R_i, i = s,o,l,os,ol$ the corresponding sideward, outward, longitudinal, out-sideward and out-long HBT radii respectively. We have suppressed the $\mathbf{K}$ dependence. We will employ the standard geometry, where the *longitudinal* direction is along the beam axis, the *outward* direction is along $\mathbf{K}_\perp$, and the *sideward* axis is perpendicular to these. Usually, each pair of particles is lorentz boosted longitudinal to the system where their rapidity vanishes, $y = 0$. Their average momentum $\mathbf{K}$ is then perpendicular to the beam axis and is chosen as the outward direction. In this system the pair velocity $\boldsymbol{\beta}_{\mathbf{K}}=\mathbf{K}/E_K$ points in the outward direction with $\beta_o = p_\perp/m_\perp$, where $m_\perp = \sqrt{m^2 + p_\perp^2}$ is the transverse mass, and the out-longitudinal coupling R_{ol} vanish at midrapidity [23]. Also R_{os} vanishes for a cylindrically symmetric source or if the azimuthal angle of the reaction plane is not determined and therefore averaged over — as has been the case experimentally so far. The reduction factor λ in Eq. (17) may be due to long lived resonances [22,24,6], coherence effects, incorrect Coulomb corrections or other effects. It is $\lambda \sim 0.5$ for pions and $\lambda \sim 0.9$ for kaons.

The Bose-Einstein correlation function can now be calculated for a deformed source. Let us first investigate *transparent* sources assuming that it is equally likely that a particle arrives at the detector from the front side of the source as from the back side, i.e., rescatterings through the source and opacities are ignored. As in [6], we parametrize the transverse and temporal extent by gaussians

$$S(x,K) \sim S_\perp(\mathrm{x},\mathrm{y}) \exp[-\frac{(\tau-\tau_f)^2}{2\delta\tau^2}]\, e^{p\cdot u/T} , \qquad (18)$$

with longitudinal Bjorken flow, $u = (\cosh\eta, 0, 0, \sinh\eta)$, as in Eq (11) without transverse flow. Effects of transverse flow will be discussed below. The transverse radii R_x, R_y are the gaussian radii at freeze-out, τ_f is the freeze-out time and $\delta\tau$ the duration of emission.

In order to calculate the correlation function of (16) the gaussian approximations is employed (see, e.g., [22,23]) which results in a correlation function of the form given in Eq. (17). Inserting the source (18) in Eq. (16) and Fourier transforming we obtain the correlation function. The HBT radii are then obtained by comparing to the experimental correlation function of Eq.(17).

It is convenient to introduce the source average of a quantity $\mathcal{O}$ defined by

$$\langle \mathcal{O} \rangle \equiv \frac{\int d^4x\, S(x,\mathbf{K})\mathcal{O}}{\int d^4x\, S(x,\mathbf{K})} \, . \qquad (19)$$

With $qx \simeq \mathbf{q}\cdot\mathbf{x} - \mathbf{q}\cdot\boldsymbol{\beta}_K\, t$ one can, by expanding Eq. (16) to second order in $q_i R_i$ and compare to Eq. (17), find the HBT radii [23]

$$R_i^2 = \langle (x_i - \beta_i\, t)^2 \rangle - \langle x_i - \beta_i\, t \rangle^2 , \qquad (20)$$

$$R_{ij}^2 = \langle (x_i - \beta_i\, t)(x_j - \beta_j\, t) \rangle - \langle x_i - \beta_i\, t \rangle \langle x_j - \beta_j\, t \rangle , \qquad (21)$$

with *i,j=s,o,l.* The HBT radii are a measure for the fluctuations [25], variance or "length of homogeneity" [26] of $(x_i - \beta_i t)$ over the source emission function $S(x,K)$. One should notice that the coordinates (x_o, x_s) are rotated with respect to the (x, y) reaction plane (see Fig. 1) by the azimuthal angle ϕ between the transverse momentum $p_\perp$ and the reaction plane. The beam axis is the same $x_l =$ z. In the local cms frame ($y = 0$) the pair velocity is $\beta_o = \beta_\perp$ whereas $\beta_s = \beta_l = 0$. All R_{ij} vanish in this frame for cylindrical symmetric sources and for an azimuthally asymmetric source only R_{os} is nonvanishing.

For transparent sources the azimuthal dependence of the HBT radii has been calculated in detail by Wiedemann [6]. In the longitudinal center-of-mass system of the pair ($y = 0$), the HBT radii are

$$R_s^2 = R^2\,[1 + \delta\cos(2\phi)] \, , \qquad (22)$$

$$R_o^2 = R^2\,[1 - \delta\cos(2\phi)] \, + \beta_o^2 \delta\tau^2 \, , \qquad (23)$$

$$R_{os}^2 = R^2 \delta \sin(2\phi) \, , \qquad (24)$$

$$R_l^2 = \frac{T}{m_\perp}(\tau_f^2 + \delta\tau^2) \, , \qquad (25)$$

where $R^2 = (R_x^2 + R_y^2)/2$ is the average of the source radii squared. One notices the characteristic modulation $\cos(2\phi)$ due to the rotation of the axes $R_{o,s}$ with respect to the reaction plane. Near target and projectile rapidities the directed flow is appreciable and leads to $\cos\phi$ terms in Eqs. (22-23) [7,6]. The out- and sideward HBT radii show a characteristic modulation as function of azimuthal angle with amplitude of same magnitude but opposite sign. Measuring the amplitude modulation of $R_{s,o,os}$ determines five quantities and thus overdetermines the three source parameters, namely the source size R, deformation δ and and duration of emission $\delta\tau$.

Next we consider *opaque* sources. In relativistic heavy ion collisions source sizes and densities are large and one would expect rescatterings. As a result particles are predominantly emitted near the surface and arrive from the (front) side of the source facing towards the detector. In [25] it was found that for opaque sources, where mean free paths are smaller than source sizes, $\lambda_{mfp}\lesssim R$, the sideward HBT radius increase whereas the outward is significantly reduced simply because the surface emission region is smaller than the whole source. As in [25,27] Glauber absorption is introduced by adding an absorption factor

$$S_{abs}(x,K) \sim \exp(-\int_x \sigma\rho(x')dx') \,, \qquad (26)$$

where σ is the interaction cross section, ρ the density of scatterers and the integral runs along the particle trajectory from source point x to the detector. Defining the mean free path as $\lambda_{mfp}=(\sigma\rho(0))^{-1}$, where $\rho(0)$ is the central density, the source is opaque when $\lambda_{mfp}\ll R$ and transparent when $\lambda_{mfp}\gg R$. Calculating the correlation function for an opaque source from Eq. (16) and comparing to the definition of the HBT radii in Eq. (17), one generally obtains for small deformations,

$$\begin{aligned} R_s^2 &= g_s R^2\left[1+\delta\cos(2\phi)\right] \,, && (27)\\ R_o^2 &= g_o R^2\left[1-\delta\cos(2\phi)\right] + \beta_o^2\delta\tau^2 \,, && (28)\\ R_{os}^2 &= g_{os} R^2\delta\sin(2\phi) \,, && (29) \end{aligned}$$

and R_l^2 is unchanged from Eq. (25). Here $g_{o,s,os}$ are model dependent factors that are functions of opacity but independent of the deformation and can be calculated as for cylindrical symmetric sources. For a gaussian source ($\rho\propto S_\perp$), which is moderately opaque ($\lambda_{mfp}/R=1$), a numerical calculation gives $g_s\simeq 1.4$ and $g_o\simeq 0.9$ (see also [27]). For a disk source with the same rms transverse radius as the gaussian radius (i.e., $R_{disk}=2R$), that emits like a black body (i.e., $\lambda_{mfp}\ll R$), one finds $g_s=4/3$ and $g_o=4(\frac{2}{3}-(\frac{\pi}{4})^2)\simeq 0.2$ [25]. Generally, $(g_s-g_o)\geq 0$ and the difference increases with opacity. Only for a completely transparent sources is $g_s=g_o$. In all cases $g_{os}\simeq g_s$. In Fig. 4 the HBT radii of Eqs. (22-29) are shown for a near-central collisions ($\delta=0.4$) with a moderate duration of emission ($\beta_o^2\delta\tau^2/g_sR^2=0.5$) for various opacities $\lambda_{mfp}/R=0.1,0.5,1.0,2.0,\infty$. As the opacity increases, g_o/g_s decreases and therefore also the outward HBT radius and its amplitude.

Comparing the HBT radii from an opaque source Eqs.(27-29) with those of a transparent source Eqs.(22-24), one notices that *the amplitudes in* R_s *and* R_o *differ* by the amount (g_s-g_o). The modulation of the HBT radii with ϕ provides five measurable quantities which over-determinates the four physical quantities describing the source: its size R, deformation δ, opacity (g_o-g_s) and duration of emission $\delta\tau$, at each impact parameter. The azimuthal dependence of the HBT radii thus offers an unique way to determine the opacity of the source as well as the duration of emission separately.

Experimentally, HBT analyses have not been combined with determination of the reaction plane yet. Consequently, the azimuthal angle ϕ is averaged and the information on three of the five measurable quantities in Eqs. (27-29) is lost. From the angular averaged difference between the out- and sideward HBT radii

$$\langle R_o^2-R_s^2\rangle_\phi = \beta_o^2\delta\tau^2-(g_s-g_o)R^2 \,, \qquad (30)$$

one can only determine the sum of the positive duration of emission and negative opacity effect. Experimentally this difference is small; NA49 [10] and NA44 [19] data even differ on the sign. Detailed analyses of the $p_\perp$ dependence of the HBT radii from NA49 data within opaque sources [27] indicate that the sources are transparent or at most moderately opaque. However, the NA44 data, for which $R_o\lesssim R_s$, requires an opaque source as seen from Eq. (30). Furthermore, the $p_\perp$ dependence of the transverse HBT radii change if the source sizes, opacities, and duration of emission also are $p_\perp$-dependent.

Transverse flow may affect the out- and sideward HBT radii as opacity, i.e., the factors $g_{o,s}$ may depend on both. For transparent sources transverse flow has been studied in [6,22,27] through Eq. (11) assuming that the transverse flow scales with transverse distance, $\mathbf{u}_\perp\simeq u_0\mathbf{r}_\perp/R$. Otherwise the same transparent gaussian source as in Eq. (18) was employed. To lowest order in the transverse flow both transverse HBT radii decrease by the same factor $\sim(1+u_0^2m_\perp/T)$ to leading order in u_0. This transverse flow correction is independent of the source size and therefore also the deformation. Consequently, spatial deformations reduce the amplitudes by the same amount in this model for both transparent (see [6]) and opaque sources. There are, however, box shape models where the transverse flow reduce R_o more than R_s [27]. A similar flow effect is found in hydrodynamic models also [35] although it is considerably less than the opacity effect, i.e., when the Cooper-Frye freeze-out condition [28] is replaced by the Bugaev freeze-out [29]. Preferrably, a transverse flow analysis of particle spectra should be performed in order to determine the magnitude of the flow so that it can be separated from opacity effects. The crucial question, however, is whether the transverse flow is azimuthally dependent, i.e., $g_{s,o}$ depend on ϕ and thereby change the amplitudes? We can estimate this effect from the elliptic flow. For a simple thermal source (18) with transverse flow as in Eq. (14), the resulting elliptic flow Eq. (15) led to a very small difference for semicentral $Pb+Pb$ collisions at SPS energies $\langle u_x^2\rangle-\langle u_y^2\rangle$ less than a few percent. Therefore, the azimuthally dependence of the flow and its effect on the amplitude in the HBT radii is also of that order only which is much less than $\delta\simeq 0.5$ for semi-central collisions. Both the deformation and elliptic flow decrease with centrality. The conclusion is that besides opacity also transverse flow may affect the factors $g_{o,s}$ - but independently of azimuthal angle. Therefore Eqs. (27-29) are still valid and can be used to extract the duration of emission unambiguously.

It is very important to measure the centrality or impact parameter dependence of the source sizes, deformation, opacity, emission times and duration of emission in order to determine how the source change with initial energy density. If no phase transition takes place one would expect that source sizes and emission times increase gradually with centrality whereas the deformation decrease approximately as in Eq. (3). In peripheral collisions, where source sizes and densities are small and few rescatterings occur, the source is transparent and the HBT radii are given by Eqs. (22-25). For near central collisions source sizes and densities are higher which leads to more rescatterings. Thus the source is more opaque and the amplitudes should differ. It would be interesting to observe this gradual change in the amplitudes with centrality. At the same time it would provide a direct experimental determination whether the source is transparent or opaque as well as extracting the magnitudes of the opacity and duration of emission separately.

V. EFFECTS OF A PHASE TRANSITION

If the matter created in an ultra-relativistic heavy ion collision undergoes a phase transition it may affect the elliptic flow and the modulation of the HBT radii. The critical energy density can be overcome either by increasing the centrality, sizes of the colliding nuclei and/or by increasing the collision energy as will be possible at the RHIC collider, $\sqrt{s} \simeq 20 \rightarrow 200$ GeV. For energy densities just above the critical value a mixed phase is created for a first order transition with zero compressibility, i.e., vanishing sound speed. Even for a second order or smooth transition, the sound speed $c_s^2 = dP/d\epsilon$ is significantly reduced according to lattice calculations [30]. The resulting transverse flow is therefore reduced [15] and should lead to smaller elliptic flow according to Eq. (12).

Unfortunately, the elliptic flow and the modulation of the HBT radii both scale with the deformation and thus decrease linearly with centrality and vanish for near central collisions, where the phase transition might occur. However, by taking the ratio of the elliptic flow to the amplitude of the HBT radii v_2/δ, the deformation cancel and the purely geometrical effects are removed. Only the collective effects as transverse flow are left to first approximation. Since the transverse flow has been found to increase with the size of the collisions system at AGS and SPS energies, we can also expect it to increase with centrality in the absence of phase transitions. In the presense of a phase transition, however, the transverse flow increase very little with centrality which results in a "plateau" in the average transverse momentum as function of centrality [31,15]. The almost constant transverse flow for centralities that produce a mixed phase should therefore according to Eq. (12) also show up in the ratio v_2/δ versus centrality such that the monotonic increase in transverse flow and v_2/δ is replaced at the critical centrality by a plateau as function of centrality as sketched in Fig. 5. The plateau extends in an interval of semi-centrality, $c_1 \rightarrow c_2$, where the pressure is constant due to a mixed phase, i.e., vanishing sound speed.

The functional dependence of v_2/δ would be similar to the van Hove prediction of the temperature as function of rapidity density [31]. Also it is similar to the *caloric curve* as was recently observed in intermediate energy nuclear collisions [32]. The caloric curve plots the temperature versus excitation energy and displays a plateau as was predicted for the liquid-gas phase transition of nuclear matter [34]. The interpretation of the caloric curve is, however, debated in the low energy community (see, e.g., [33]).

If a phase transition occurs at some centrality, where energy densities exceed the critical value, one may also observe sudden changes in the physical quantities measured in HBT analyses. The emission time and duration of emission increase drastically in hydrodynamic calculations [35] leading to very large R_l and R_o (see also Fig. 5). A long lived mixed phase would also emit particles as a black body and thus the opacity increase and the opacity factor g_o/g_s decrease as shown in Fig. 5. If droplet formation occurs leading to rapidity fluctuations, one may be able to trigger on such fluctuations and find smaller longitudinal and sideward HBT radii [36].

Alternatively, one could plot the quantities as function of collision energy or size of the colliding nuclei for fixed centrality with a similar qualitative dependence of the physical quantities with and without a phase transition. Furthermore, if an interesting change in these quantities should occur at some centrality or collision energy, it would also be most interesting to look for simultaneous J/Ψ suppression [37], strangeness enhancement, decrease in directed, elliptic or transverse flow, or other signals from a phase transition.

VI. SUMMARY

In summary, measuring the reaction plane in relativistic nuclear collisions, the elliptic flow and HBT radii simultaneously gives a detailed description of the source at freeze-out as well as how the source expands in space and time from the initial collision and up to freeze-out.

The elliptic flow was calculated in the collisionless limit from the Boltzmann equation with a collision term as well as in the hydrodynamic limit assuming equipotential flow. The collisionless limit is expected to be valid for peripheral collision where few rescatterings are expected. Alternatively, the hydrodynamic limit is expected to be valid for central collision where many rescatterings are expected. For small transverse source deformations the elliptic flow is proportional to the deformation in both limits. Detailed cascade and 3+1 dimensional hydrodynamic calculations are clearly needed of both the radial and elliptic flow as well as HBT radii for non-central nuclear collisions with and without phase transitions.

The estimates in the collisionless limit of Eq.(9) give a reasonable description of both the magnitude and $p_\perp$-dependence of the elliptic flow measured at SPS energies in $Pb + Pb$ semicentral collisions for both pions and protons. Furthermore, the measured elliptic flow is largest at midrapidies and is approximately proportional to dN/dy as also predicted by Eq.(9). In the hydrodynamic limit transverse flow couples to $p_\perp$ and elliptic flow is therefore expected to be the same for all particles at the same $p_\perp$. For equipotential flow given by Eq. (12) can also describe the proton elliptic flow , however, with a deformation is a factor ~ 7 smaller than the initial deformation of the collision zone. It is expected to be somewhat smaller due to expansion between initial collision and freeze-out. The measured elliptic flow for pions lies between the collisionless and hydrodynamic limit as could be expected since the particle mean free paths are a few *fermi*'s — comparable to the transverse source sizes for $b = R_{Pb} \simeq 7$ fm/c. Comparing the $p_\perp$-dependence of elliptic flow for pions and protons reveals distinctively the change from collisionless expansion to hydrodynamic flow. In the collisionless limit they differ (see Fig. 3) whereas in the hydrodynamic limit they should become the same.

The modulation of the HBT radii with azimuthal angle between the reaction plane and particle transverse momenta can be exploited to obtain source sizes, deformations, life-times, duration of emission and opacities separately. HBT radii provides important space-time information which complements the momentum space information from particle spectra on elliptic flow during expansion and freeze-out. The HBT radii can distinguish between opaque sources Eqs.(27-29) from transparent source Eqs.(22-24) because *the amplitudes in R_s and R_o differ.* The modulation of the HBT radii with ϕ provides five measurable quantities which over-determinates the four physical quantities describing the source: its size R, deformation δ, opacity $(g_o - g_s)$ and duration of emission $\delta\tau$, at each impact parameter. The azimuthal dependence of the HBT radii thus offers an unique way to determine the opacity of the source as well as the duration of emission separately.

Tracking these physical quantities with centrality will provide detailed information about the source created in relativistic nuclear collisions and may reveal a phase transition as sketched in Fig. (5).

ACKNOWLEDGMENTS

Discussions with G. Baym, I. Bearden, J.J. Gårdhøje, U. Heinz, P. Huovinen, R. Mattiello, L. McLerran, D. Rischke, V. Ruuskanen and S. Voloshin are gratefully acknowledged. Special thanks to A. Poskanzer for comments and the improved NA49 data [3].

APPENDIX A: Evaluation of the Collision Integral

In order to calculate the elliptic flow, we need the particle distribution integrated over space for normalization in Eq. (5). With the free streaming distribution function of Eq. (7) we find at any time τ

$$\frac{dN_1}{dyd^2p_\perp} = (2\pi)^{-3}\int m_\perp \cosh(\eta - y) n(r,p,t)\tau d\eta d^2r_\perp = (2\pi)^{-3}\tau_0 \int dp_z\, f_0(p_\perp, p_z)\,. \tag{31}$$

The change of particle momenta due to collisions is the change in the particle distribution function integrated over space and time

$$\frac{d\Delta N_1}{dyd^2p_\perp} = \frac{E_1}{(2\pi)^3}\int \left(\frac{\partial n}{\partial t}\right)_{coll} dt\, d^3r\,. \tag{32}$$

In the collisionless limit we can now insert the free streaming distribution function (7) in the collision term in order to calculate the first order correction to the distribution function. As will be shown below, the system expands rapidly to low densities, where collisions mainly contribute, and therefore the final state factors $(1 \pm n_i)$ from stimulated emission/Pauli blocking can be ignored. For small angle scatterings the loss and gain terms in $(n_3n_4 - n_1n_2)$ nearly cancel leading to a suppression factor at forward and backward angles $\sim (1 - \cos^2\theta)$. Furthermore, little momentum is lost in small angle deflections leading to little deformation in momentum space. We therefore replace the cross section by an angular and energy averaged *transport* cross section σ_{tr} and keep only the loss term $\propto n_1n_2$

$$\frac{d\Delta N_1}{dyd^2p_\perp} = -\frac{E_1}{(2\pi)^3}\int d^2r_\perp \tau d\tau d\eta \int \frac{d^3p_2}{(2\pi)^3} v_{12}\sigma_{tr}\, n_1n_2\,, \tag{33}$$

where we have changed variables to the space-time rapidity and invariant time.

At late times we can utilize that the free streaming distribution longitudinally can be approximated by

$$f_0(p_\perp, p'_z) \simeq \frac{\tau_0}{\tau} m_\perp^{-1}\delta(y - \eta)\int dp_z f_0(p_\perp, p_z)\,. \tag{34}$$

where the latter integral can be eliminated by use of Eq. (31). The resulting free streaming distribution function of Eq. (7) becomes

$$n(x,p) \simeq S_\perp(\mathbf{r}_\perp - \mathbf{v}_\perp\tau')\frac{(2\pi)^3}{\tau m_\perp}\delta(y - \eta)\frac{dN}{dyd^2p_\perp}\,. \tag{35}$$

First we deal with the integration over transverse coordinates

$$I_\perp \equiv \int d\mathrm{x}d\mathrm{y}\, S_\perp(\mathbf{r}_\perp - \mathbf{v}_{1\perp}\tau')\, S_\perp(\mathbf{r}_\perp - \mathbf{v}_{2\perp}\tau')$$
$$= \frac{1}{4\pi R_x R_y} \exp\left[-\frac{\tau'^2}{4R_x^2}(v_{1x}-v_{2x})^2 - \frac{\tau'^2}{4R_y^2}(v_{1y}-v_{2y})^2 \right] ,$$

with $\tau' = \tau - \tau_0$. The transverse particle momentum or velocity with respect to the reaction plane (x-axis) is $\mathbf{v}_{1\perp} = (v_{1x}, v_{1y}) = v_{1\perp}(\cos\phi, \sin\phi)$, in terms of the azimuthal angle ϕ. Assuming deformations are small we obtain by expanding in δ

$$I_\perp = \frac{1}{4\pi R_x R_y} \exp\left[-\frac{\tau'^2 v_{12}^2}{4\bar{R}^2} \right] \times \left(1 - \frac{\tau'^2 v_{1\perp}^2}{4\bar{R}^2} \delta \cos(2\phi) \, + \, \mathcal{O}(\delta^2) \right) . \quad (36)$$

where $v_{12} = |\mathbf{v}_{1\perp} - \mathbf{v}_{2\perp}|$ is the relative velocity. At this point we make the important observation that the asymmetric term proportional to $\cos(2\phi)$ is weighted by a factor $\tau'^2 = (\tau - \tau_0)^2$, i.e., scatterings at early times contribute little to azimuthal asymmetries in the momentum distribution whereas they are important around $\tau \sim 2\bar{R}/v_{12}$. This justifies Eqs. (34) and (35) as well as the neglect of the Bose and Fermi factors $(1 \pm n_i)$ in the collision term as densities are low at late times. The physical reason for the "late time" dominance in elliptic flow is that particles have to travel a distance $\sim R$ before it feels the source deformation, i.e., whether it moves in the x− direction, where $R_x < R$, or in the y− direction, where $R_y > R$.

Since $\tau_0 \ll \bar{R}/v_\perp$, the time integral becomes

$$\int_{\tau_0}^{\infty} \frac{d\tau}{\tau} I_\perp = -\frac{\delta}{8\pi R_x R_y} \frac{v_{1\perp}^2}{v_{12}^2} \cos(2\phi) + constant , \quad (37)$$

where the constant is independent of azimuthal angle ϕ. Finally, we carry out the p_2 and $d\eta$ integrals in Eq. (33) using (37) with the result

$$\frac{d\Delta N_1}{dyd^2p_\perp} = \langle v_{12}\sigma_{tr} \rangle \frac{dN_2}{dy} \frac{dN_1}{dyd^2p_\perp} \frac{\delta}{8\pi R_x R_y} \frac{v_{1\perp}^2}{\langle v_{12}^2 \rangle} \cos(2\phi) + constant , \quad (38)$$

where the averaging over scatterer momenta is indicated by $\langle .. \rangle$. Originally we only included loss terms in the Boltzmann equation and thereby replaced the cross section by the transport cross section. The gain terms will not affect the asymmetric term but will cancel the constant term in Eq. (38) when the number of particles is conserved. If there is net particle absorption or production, v_2 should be multiplied by the ratio of initial and final particle number.

We can now generalize to several kind of scatterers by replacing 1 by a given particle species i as pions, protons, etc. and replace the scatterer 2 by a sum of scatterers j. By dividing Eq. (38) by $dN_1/dyd^2p_\perp$ we obtain by comparing to the definition, Eq. (5), of elliptic flow

$$v_2^i = \frac{\delta}{16\pi R_x R_y} \sum_j \langle v_{ij} \sigma_{tr}^{ij} \rangle \frac{dN_j}{dy} \frac{v_{i\perp}^2}{v_{i\perp}^2 + \langle v_{j\perp}^2 \rangle} . \quad (39)$$

APPENDIX B: Evaluation of equipotential flow in semi-central collisions

In this appendix we evaluate the elliptic flow for an asymmetric source with equipotential flow which is parametrized spatially as a gaussian in transverse directions. We assume particles are thermally distributed with local flow velocity $\mathbf{u}_\perp$ as in Eq. (11). By assumption the transverse flow is constant on the freeze-out surface which is determined by

$$a^2 = \frac{\mathrm{x}^2}{R_x^2} + \frac{\mathrm{y}^2}{R_y^2} . \quad (40)$$

i.e., $u_\perp$ is a function of a but independent of the azimuthal angle $\phi' = \tan^{-1}(\mathrm{y}/\mathrm{x})$. Also, the transverse flow velocity is perpendicular to the elliptic surface

$$\mathbf{u}_\perp = u_\perp \mathbf{n} = u_\perp(a) \frac{\left(R_y^2 \cos\phi', R_x^2 \sin\phi' \right)}{\sqrt{R_y^4 \cos^2\phi' + R_x^4 \sin^2\phi'}} . \quad (41)$$

In calculating the azimuthal dependence only the transverse directions are important as normalizations cancel in Eq. (5). Thus

$$\frac{dN}{dyd^2p_\perp} \propto \int a da S_\perp(a) \int d\phi' \, \exp(\mathbf{u}_\perp \cdot \mathbf{p}_\perp / T) . \quad (42)$$

Expanding for small deformations we obtain

$$\frac{dN}{dyd^2p_\perp} \propto \langle I_0 (\frac{p_\perp u_\perp}{T} [1 + \delta \cos(2\phi)]) \rangle , \quad (43)$$

where the average $\langle .. \rangle$ refers to radial average over a of the transverse flow. I_0 is the Bessel function of imaginary argument which has the limits

$$I_0(x) = \left\{ \begin{array}{ll} 1 + \frac{1}{4}x^2 & , \ x \ll 1 \\ \exp(x)/\sqrt{2\pi x} & , \ x \gg 1 \end{array} \right\} . \quad (44)$$

Expanding for small deformations and comparing to the definition of elliptic flow (5) we finally obtain

$$v_2 = \left\{ \begin{array}{ll} \frac{1}{4} \frac{p_\perp^2 \langle u_\perp^2 \rangle}{T^2} \delta & , \ p_\perp u_\perp \ll T \\ \frac{1}{2} (\frac{p_\perp \langle u_\perp \rangle}{T} - 1) \delta & , \ p_\perp u_\perp \gg T \end{array} \right\} . \quad (45)$$

APPENDIX C: Apparent Temperatures and Transverse Flow

Transverse flow affects the measured $p_\perp$ and $m_\perp$ slopes. The *apparent* temperatures, obtained by fitting the particle spectra by $dN/d^2p_\perp \propto \exp(-m_\perp/T_{app})$, are larger than the intrinsic ones. It is difficult to determine the intrinsic temperature and the transverse flow separately from $p_\perp$ slopes of pions alone [38]. Recent measurements [16] of apparent temperatures for various massive particles, $\pi, K, p, d, ^3He$, etc, may allow us to estimate the transverse flow uniquely as will now be described.

Assume a thermal source in two dimensions with intrinsic temperature T at freeze-out and (transverse) flow $u_\perp$ locally. i.e., $n \sim exp(p \cdot u/T)$. For small transverse deformations the flow is almost azimuthally symmetric and its average value is equal to the cylindrical symmetric value, $u_\perp(r)$. The distribution of particles is thus

$$n(r,p,t) \sim \exp[\frac{-\gamma m_\perp + \mathbf{p}_\perp \cdot \mathbf{u}_\perp}{T}] \,. \tag{46}$$

In three dimensions the source is further complicated by the thermal factor $\exp(-m_\perp \cosh(y-\eta)/T)$. After integrating over longitudinal direction or η, however, the result are very similar when $m_\perp \gg T$.

The dependence on the angle θ between $\mathbf{p}_\perp$ and $\mathbf{u}_\perp$ in Eq. (46) is crucial. Integrating over transverse coordinates gives the distribution

$$\frac{dN}{d^2p_\perp} \propto \exp[-\gamma \frac{m_\perp}{T}] \langle I_0(p_\perp u_\perp/T) \rangle \,, \tag{47}$$

where $\langle ... \rangle$ refers to radial average of the transverse flow and I_0 the Bessel function (see Eq.(44).

The apparent temperature defined as the inverse $m_\perp$ slope becomes

$$\begin{aligned} T_{app} &\equiv [-\frac{d}{dm_\perp} \ln(\frac{dN}{d^2p_\perp})]^{-1} \\ &= \left\{ \begin{array}{ll} T + \frac{1}{2} m_\perp \langle u_\perp^2 \rangle & , \; p_\perp u_\perp \ll T \,, \, m_\perp u_\perp^2 \ll T \\ T\sqrt{\gamma - u_\perp} & , \; p_\perp u_\perp \gg T \,, \, p_\perp \gg m \end{array} \right\} . \end{aligned} \tag{48}$$

At small $p_\perp$ the result is the expected one when the kinetic energy of flow is added to the thermal energies in two dimensions. At large $p_\perp$ and flow one instead obtains the *blueshift* formula [39]. Experimentally, the apparent temperature is determined by exponential fits to $dN/d^2p_\perp$ in a certain region of $p_\perp$ and it may therefore differ somewhat from (48).

One should notice that in experimental fits to particle spectra the apparent temperatures are parametrized as $T_{app} = T + m\beta^2$. Consequently, this flow parameter differs from ours by a factor: $\beta^2 = \langle u_\perp^2 \rangle/2$.

[1] W. Reisdorf and H.G. Ritter, *Ann. Rev. Nucl. Part. Sci.* **47** (1997) 663.

[2] E877 coll., J. Barrette et al., *Phys. Rev.* **C56** (1997) 3254; E895 coll., H. Liu et al., **A638** (1998) 451c.

[3] H. Appelshäuser et al. (NA49), *Phys. Rev. Lett.* **80**, 4136 (1998). A. Poskanzer (NA49), *Nucl. Phys.* **A638** (1998) 463c. Improved data from na49info.cern.ch home page has been employed.

[4] R. Hanbury–Brown and R.Q. Twiss, *Phil. Mag.* **45** (1954) 633.

[5] S.A. Voloshin, *Phys. Rev.* **C55** (1997) R1630; A.M. Poskanzer and S.A. Voloshin, *Phys. Rev.* **C58** (1998) 1671.

[6] U. Wiedemann, *Phys. Rev.* **C57**, 266 (1998).

[7] J.Y. Ollitrault, *Phys. Rev.* **D46** (1992) 229; *ibid.* **D48** (1993) 1132; and Proc. of QM'97.

[8] H. Sorge, *nucl-th/9610026.*

[9] H. Liu, S. Panitkin, and N. Xu, *nucl-th/980721.*

[10] T. Alber et al., *Z. Phys.* **C 66** (1995) 77; K. Kadija et al., *Nucl. Phys.* A 610 (1996) 248c; R. Ganz et al., *nucl-ex/9808006.*

[11] H.W. Barz, J. Bondorf, J.J. Gårdhøje, and H. Heiselberg, *Phys. Rev.* **C56** (1997) 1553; *ibid* **C57** (1998) 2536.

[12] L.W. Nordheim, *Proc. Roy. Soc.* (London) V, **A119** 689 (1928).

[13] G. Baym, *Phys. Lett.* **138B**, 18 (1984). H. Heiselberg and X.-N. Wang, *Phys. Rev.* **C53**, 1892 (1996).

[14] G. Baym, B. Friman, J.-P. Blaizot and M. Soyeur, *Nucl. Phys.* **A407**, 541 (1983).

[15] M. Kataja, P.V. Ruuskanen, L.D. McLerran, H.von Gersdorff, *Phys. Rev.* **D34** (1986) 2755.

[16] I.G. Bearden et al. (NA44 collaboration), *Phys. Rev. Lett.* **78** (1997) 2080.

[17] H.W. Barz, G. Bertsch, P. Danielewicz and H. Schulz, *Phys. Lett.* **B 275**, 19 (1992).

[18] H. Heiselberg, nucl-th/9809077, to appear in *Phys. Rev. Lett.* (1999).

[19] A. Franz, *Nucl. Phys.* **A 610** (1996) 240c. I.G. Bearden et al., *Phys. Rev.* **C58** (1998) 1656.

[20] M. Gyulassy, S.K. Kaufmann and L.W. Wilson, *Phys. Rev.* **C 20** (1979) 2267.

[21] S. Pratt, *Phys. Rev. Lett.* **53** (1984) 1219.

[22] T. Csörgő and B. Lörstad, *Nucl. Phys.* **A590**, 465c (1995); *Phys. Rev.* **C54** (1996) 1390.

[23] S. Chapman, J.R. Nix, and U. Heinz, *Phys. Rev.* **C52**, 2694 (1995).

[24] H. Heiselberg, *Phys. Lett.* **B379** (1996) 27. U.A. Wiedemann and U. Heinz, *Phys. Rev.* **C56** (1997) 3265.

[25] H. Heiselberg and A.P. Vischer, *Eur. Phys. J.* **C1**, 593 (1998); *Phys. Lett.* **B421** (1998) 18;

[26] Yu. M. Sinyukov, V.A. Averchenkov, B. Lörstad, *Z. Phys.* **C49** (1991) 417.

[27] B. Tomasik and U. Heinz, nucl-th/9805016.

[28] F. Cooper and G. Frye, *Phys. Rev.* **D10** (1974) 186.

[29] K.A. Bugaev, *Nucl. Phys.* **A606** (1996) 559.

[30] C. Bernard et al., *Phys.Rev.* **D55** (1997) 6861.

[31] L. Van Hove, it Phys. Lett. **118B** (1982) 138.

[32] J. Pochodzalla et al. (ALADDIN), *Phys. Rev. Lett.* **75**, 1040 (1995).

[33] J.A. Hauger et al., *Phys. Rev. Lett.* **77** (1996) 235.

[34] J.P.Bondorf, R. Donangelo, I.N. Mishustin and H. Schulz, *Nucl. Phys.* **A444** (1985) 460.

[35] S. Bernard, D.H. Rischke, J.A. Maruhn, W. Greiner *Nucl. Phys.* **A625**, 473 (1997).

[36] H. Heiselberg and A.D. Jackson, *nucl-th*/9809013.

[37] H. Heiselberg and R. Mattiello, *nucl-th*/9901004.

[38] E. Schnedermann and U. Heinz, *Phys. Rev. Lett.* **69** (1992) 2908.

[39] P.V. Ruuskanen, *Z. Phys.* **C38** (1988) 219.

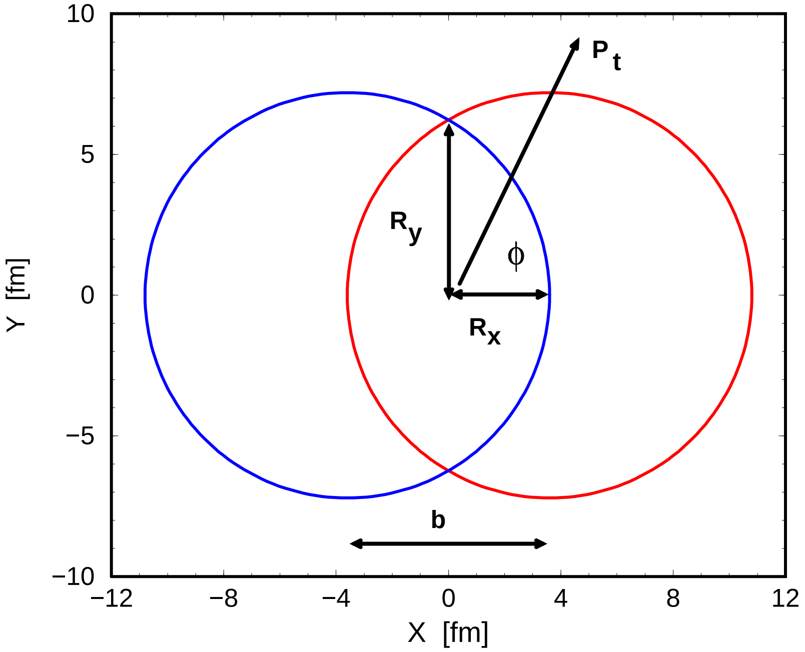

FIG. 1. Reaction plane of semi-central $Pb + Pb$ collision for impact parameter $b = R_{Pb} \simeq 7$fm. The overlap zone is deformed with $R_x \leq R_y$. The reaction plane (x, z) is rotated by the angle ϕ with respect to the transverse particle momentum $p_\perp$ which defines the outward direction in HBT analyses.

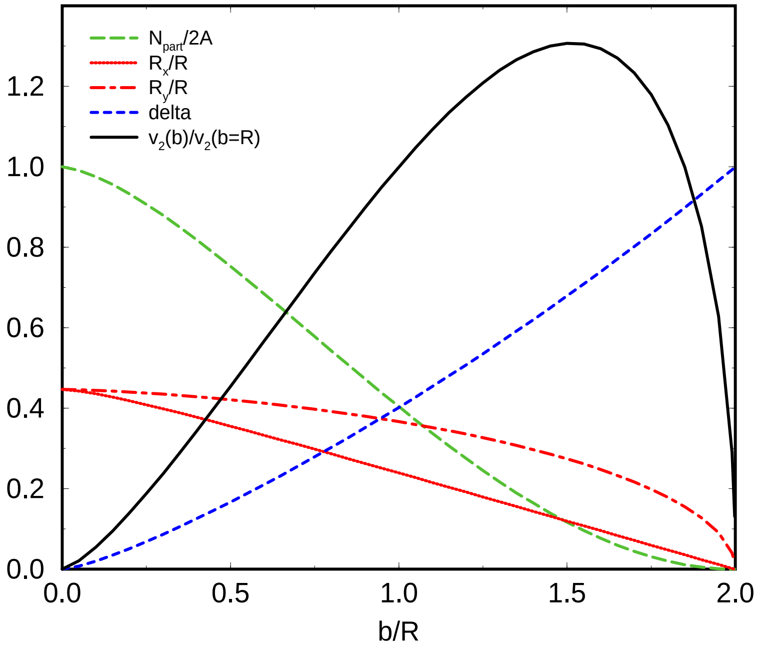

FIG. 2. Transverse radii of nuclear overlap, deformation, number of participants and elliptic flow parameter (see Eq.(9) and text) versus impact parameter.

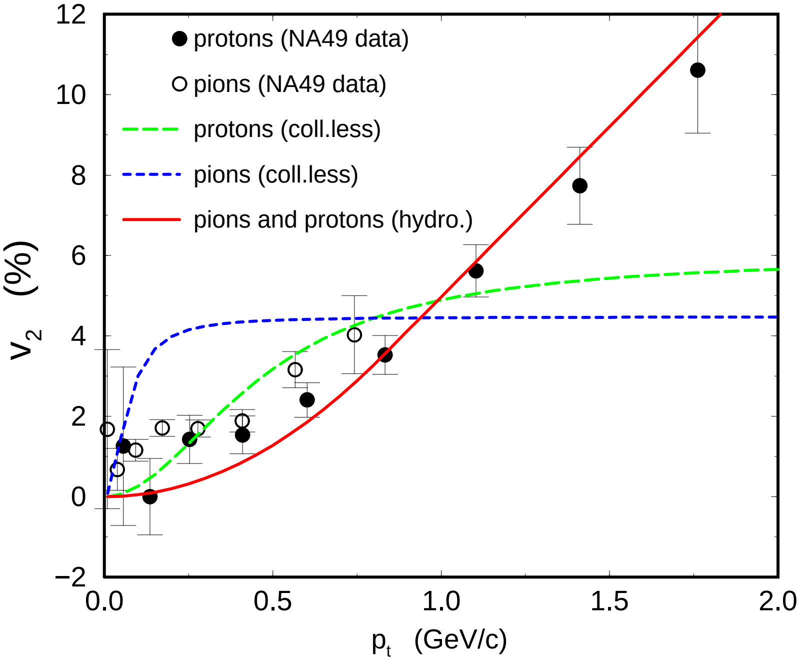

FIG. 3. Elliptic flow v_2 for pions and protons versus transverse momentum. Data from NA49 [3]. Curves represent hydrodynamic limit of Eq.(12) (full curve) and collisionless limit of Eq.(9) for pions (dashed) and protons (dotted) (see text for details).

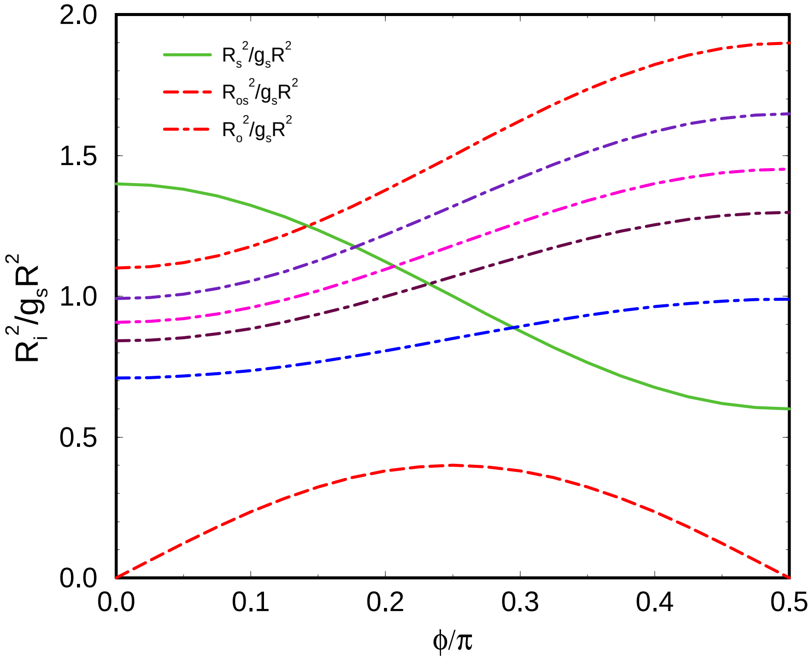

FIG. 4. HBT radii vs. angle between reaction plane and transverse particle momenta. The HBT radii are normalized to the angle averaged sideward HBT radius squared, g_sR^2, for deformed $\delta = 0.4$ source with duration of emission $\beta_o^2\delta\tau^2/g_sR^2 = 0.5$ and with various opacities. The sideward HBT radius (full curve) is then the same for both transparent (Eq. (22)) and opaque (Eq. (27)) sources and likewise for the out-side HBT radii (Eqs. (24) and (29), dashed curve). The outward HBT radii are shown with chain-dashed curves for a gaussian source (Eq. (28) and (23) with various opacities (from below and up): $\lambda_{mfp}/R = 0.1, 0.5, 1.0, 2.0, \infty$.

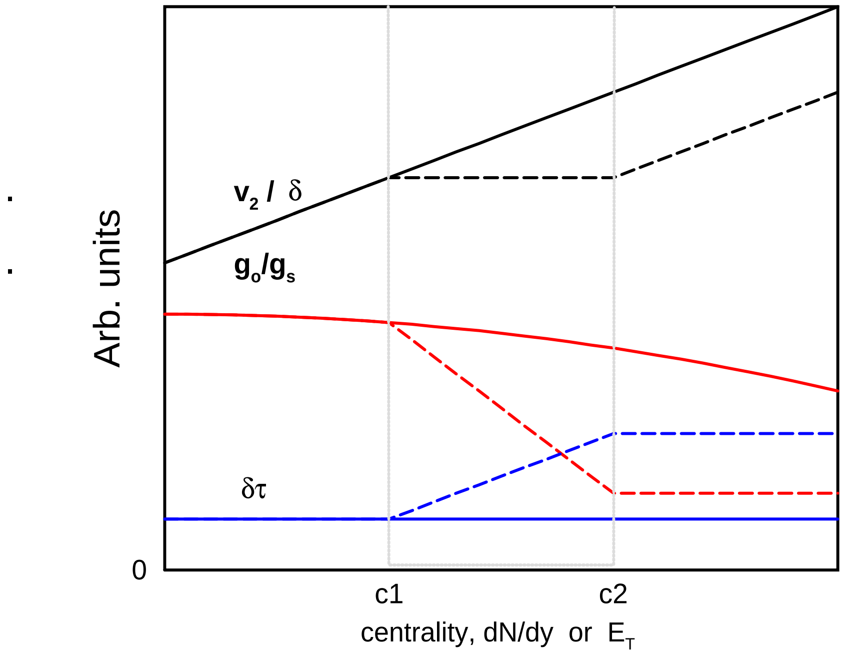

FIG. 5. Skematic behavior of the centrality, dN/dy or E_T dependence with and without a phase transition. From top to bottom the curves show the ratio of elliptic flow to deformation v_2/δ, opacity g_o/g_s, and duration of emission $\delta\tau$. The expected behavior without (full curves) and with (dashed curves) a first order phase transition occurring in a region of semi-centrality from $c1$ to $c2$ is described in the text.